RSC Advances

PAPER

View Article Online
View Journal | View Issue

Cite this: *RSC Adv.*, 2021, **11**, 39768

Matrix-dispersed magnetic molecularly-imprinted polyaniline for the effective removal of chlorpyrifos pesticide from contaminated water

Hadeel Saad,†[a] F. A. Nour El-Dien, *[a] Nadia E. A. El-Gamel[a] and Ahmed S. Abo Dena *[bc]

Received 23rd October 2021
Accepted 6th December 2021

DOI: 10.1039/d1ra07833j

rsc.li/rsc-advances

We report a new adsorbent nanocomposite material based on matrix-dispersed superparamagnetic iron oxide nanoparticles (SPIONs) in molecularly-imprinted polyaniline for the removal of chlorpyrifos (CPF), a hazardous organophosphate pesticide, from water. The synthesized magnetic molecularly-imprinted polymer (MMIP) was characterized by FTIR spectroscopy, XRD, magnetic susceptibility, DLS, zeta potential measurement, SEM and high-resolution TEM imaging. The average size of the naked SPIONs ranges from 15 to 30 nm according to the high-resolution TEM analysis. Moreover, the adsorption kinetics, thermodynamic parameters (ΔG, ΔH and ΔS), adsorption isotherms and rebinding conditions were investigated in detail. The proposed MMIP has an imprinting factor of 1.64. In addition, it showed a high experimental adsorption capacity of 1.77 mg g^{-1} and a removal efficiency of nearly 80%. The fabricated MMIP material demonstrated excellent magnetic susceptibility allowing for easy separation using an external magnetic field. The adsorption mechanism of CPF onto the MMIP adsorbent followed the second-order kinetics model and fitted to the Temkin adsorption isotherm. By studying the adsorption thermodynamics, negative ΔG values (−1.955 kJ mol^{-1} at room temperature) were obtained revealing that the adsorption process is spontaneous. Furthermore, the maximum adsorption capacity was obtained at room temperature (*ca.* 303 K), neutral pH and using a high CPF concentration.

Introduction

Water pollution has become one of the most serious issues facing people at the present time, especially with the huge population increase that requires a corresponding increase in drinking and irrigation water resources. The global water crisis is not only due to the scarcity of water resources, but also due to the progressive deterioration of water quality that leads to noticeable reduction in the quantity of water suitable for safe use. There is a tight link between the global water-quality crisis and agriculture due to the heavy use of pesticides/herbicides for agricultural purposes, causing serious contamination to a large amount of municipal/surface water. In addition, agricultural causalities of water pollution have overtaken industrial and/or settlement-based contaminations. On the other hand, the increasing food demand intensifies the agricultural pressure on the global water quality. Nutrients/fertilizers, pesticides, herbicides, fungicides, salts, sediments, metals, organic matter, pathogens (*e.g.* bacteria), drug residues, hormones and feed additives are the major agricultural sources of surface municipal water pollution.

Acute poisoning with highly hazardous pesticides, used by poor farmers in developing countries, can cause significant human/animal mortality and morbidity worldwide.[1] From these pesticides, chlorpyrifos (CPF; IUPAC name: *O*,*O*-diethyl *O*-3,5,6-trichloro-2-pyridyl phosphorothioate; molar mass: 350.6 g mol^{-1}) is one of the most hazardous organophosphate pesticides (Scheme 1). Although CPF has low solubility in water at room temperature (6.36 ± 0.58 mg L^{-1}),[2] it is considered one of the most hazardous water contaminants due to its very high toxicity. Therefore, due to the sustained discharge of CPF from soil to water, it is necessary to develop new selective, efficient and cost-effective sorbents for the removal of CPF from water.

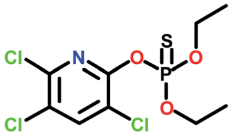

Scheme 1 Chemical structure of CPF.

---

[a]Chemistry Department, Faculty of Science, Cairo University, Giza 12613, Egypt

[b]Pharmaceutical Chemistry Department, National Organization for Drug Control and Research (NODCAR), Giza, Egypt

[c]Faculty of Oral and Dental Medicine, Future University in Egypt (FUE), New Cairo, Egypt

† Present address: Egyptian Chemistry Administration, Ramses street, Cairo, Egypt.

The emergence of enzyme-analog built polymers, nowadays known as molecularly-imprinted polymers (MIPs), in the 1970s introduced a new kind of target-specific polymeric materials.[3–7] These materials have found a very wide range of applications in different areas, including chemical sensing,[8–13] adsorption,[14–16] catalysis,[17] biology,[18] *etc.* Combining MIPs with superparamagnetic iron oxide nanoparticles (SPIONs) enables the control of the produced nanocomposites using an external magnetic field.[19] SPIONs also provide the advantages of being biocompatible and easy-to-synthesize.[20] Recently, the attention of many researchers has been grasped by the use of magnetic nanomaterials for the removal of hazardous contaminants, including pesticides, from water.[21–24] The removal of CPF from water *via* bioremediation,[25–28] Fenton reaction,[29–33] graphitic carbon nitride-incorporated chitosan[34] and metal nanoparticles[35] was reported in the literature. CPF-selective MIPs and magnetic MIPs (MMIPs) were also reported using different kinds of polymers either for extraction/pre-concentration or removal of CPF.[36–39] Most of these MIPs/MMIPs are based on functional monomers that require a high-temperature medium and a very long polymerization time. In addition, crosslinking agents and inert atmospheres are often required. Some studies reported the use of molecularly-imprinted polyaniline (PANI) for various applications including water treatment,[40–42] sensor applications,[43,44] *etc.* The recent interest in PANI applications is due to its unique properties which include, but are not limited to, the ease of fabrication, low cost, high stability, high electrical conductivity, *etc.* Besides, PANI preparation does not require a high-temperature polymerization medium nor a cross-linking agent.

The objective of the present study is to prepare a MMIP-based nanocomposite adsorbent for the effective and selective removal of CPF from contaminated water. The proposed MMIP nanomaterial is based on SPIONs dispersed in an imprinted PANI matrix. Bulk polymerization of aniline is very rapid and takes place at low temperature; thus allowing for facile scaling up of the MMIP-fabrication process. In the following sections, the MMIP preparation procedure, characterization techniques and CPF adsorption experiments will be discussed.

Materials and methods

Materials

Chlorpyrifos, a product of Excel Crop Care Limited, was provided by El Nasr for Intermediate Chemicals (Egypt) and was used as a template. For the synthesis of the molecularly imprinted polyaniline, aniline (Al-Alamia for Chemical Industries, Egypt), dimethyl sulphoxide (Oxford Lab Fine Chem LLP, India) and ammonium persulphate (APS, Veb-Laborchemie Apolda, Germany) were used. Ethylene glycol (Honeywell International Inc., USA), ferric chloride hexahydrate ($FeCl_3 \cdot 6H_2O$, Daejung Chemicals and Metals, South Korea) and anhydrous sodium acetate (ADWIC, Egypt) were utilized in the solvothermal synthesis of SPIONs. Ethyl alcohol was obtained from the International Company for Medical Industries (Egypt), methyl alcohol and hydrochloric acid were purchased from Alpha Chemika (India), and glacial acetic acid was provided by Piochem (Egypt). All reagents were of analytical grade and were used without any further purification.

Instrumentation

An evolution 60 Thermo Scientific Spectrophotometer (USA) was used to detect/quantify the concentration of CPF at 290 nm using a 1 cm quartz cell. To study the surface morphology and particle size, field-emission scanning electron microscopy (FE-SEM) and high-resolution transmission electron microscopy (HRTEM) were used with the aid of a VEGA3 TESCAN (Czech Republic) and JEOL JEM-2100 (Japan), respectively. The particle size and zeta potential (ZP) of naked SPIONs and MMIPs were determined by a Malvern Panalytical instrument (UK). Fourier transform infrared spectra (FTIR) were recorded using a Nicolet 6700 ATR-FTIR spectrometer (Thermo Scientific, Germany). The magnetic properties were investigated with a vibrating-sample magnetometer (VSM) (Lakeshore, model 7410). Magnetite crystallographic structure was confirmed by measuring the X-ray diffraction (XRD) spectra (Discover-D8, Bruker, USA).

Preparation of SPIONs

Superparamagnetic Fe_3O_4 nanoparticles were prepared *via* the modified solvothermal method.[45,46] Briefly, 2 g of $FeCl_3 \cdot 6H_2O$ and 6 g of anhydrous sodium acetate were dissolved in 65 mL of ethylene glycol. This solution was transferred to a Teflon-lined solvothermal reactor and then heated to 200 °C in the oven (Heraeus, Thermo Electron Corporation, Germany) for 12 h. The prepared black magnetite nanoparticles were left to cool at room temperature, separated with an external magnet, washed several times using distilled water and ethanol to effectively remove the solvent, and then vacuum dried at room temperature for 24 h. The solvothermal reactor must be completely dry to prevent the formation of any iron oxide but magnetite.

Preparation of MMIPs

First, 1 mL (*ca.* 10.95 mmol) of aniline as a functional monomer and 1 g of SPIONs were mixed in 25 mL of HCl (1 mol L^{-1}) and stirred constantly at 4 °C. Thereafter, 0.96 g (*ca.* 2.74 mmol) of CPF – as a template – were dissolved in 20 mL of DMSO and added to the above mixture in a dropwise manner with constant stirring.[47] After mixing, 1.21 g (*ca.* 5.48 mmol) of APS – as an initiator – were dissolved in 5 mL of 1 mol L^{-1} HCl and dropped onto the mixture for about 1 h with constant stirring. The solution was stirred continuously for 6 h in an ice bath. The appearance of a dark green color indicates the formation of emeraldine salt of polyaniline (PANI), Fig. 1. Magnetic non-imprinted polymer (MNIP) was prepared by following the same procedure but without the addition of the template, CPF.

The obtained PANI/SPIONs nanocomposite was collected from the suspension with a strong magnet, and then washed thrice with distilled water. Subsequently, CPF was removed

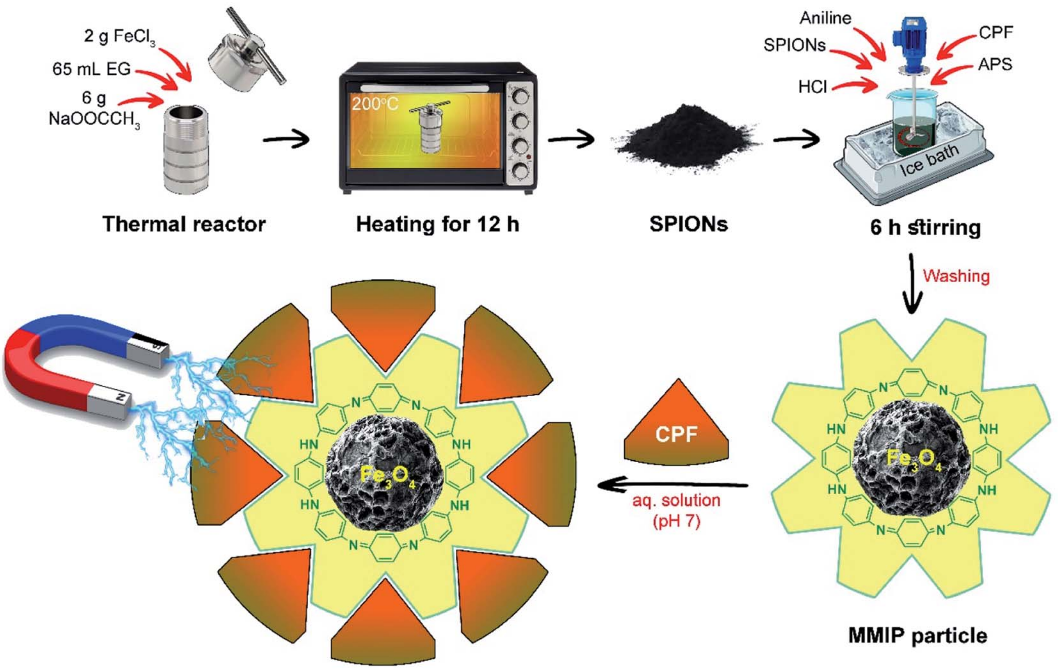

Fig. 1 Schematic illustration summarizing the synthetic steps of the MMIP and its use in the treatment of CPF-contaminated water at neutral pH.

from the PANI/SPIONs nanocomposite *via* repeated washing with a mixture of methanol and 1% acetic acid solution (9 : 1, v/v) until no CPF could be detected spectrophotometrically at 290 nm, and then the resultant solid was washed several times with methanol to remove the excess acid. The resulting MMIP was left overnight to dry at room temperature. It is worth mentioning that the prepared MNIP was treated similarly to minimize any systematic errors.

Adsorption experiments

The adsorption of CPF in aqueous solution was studied by the batch-mode adsorption technique. All the adsorption experiments were carried out in 50 mL glass-stoppered Erlenmeyer flasks containing 0.2 g of the adsorbent and 10 mL of CPF solution of the appropriate concentration at room temperature. The suspension was placed in a temperature-controlled shaker (Clifton, UK) with a shaking speed of 400 rpm. Working CPF solutions (15–45 mg L^{-1}) were prepared shortly before each experiment by dilution of a 1000 mg L^{-1} CPF stock solution with a methanol/water mixture (3 : 7, v/v).

The effect of pH on CPF adsorption was studied by using working solutions of different pH values (pH 2–10) adjusted by 0.1 mol L^{-1} hydrochloric acid and sodium hydroxide solutions. The pH of the prepared solutions was measured using a JENCO 6173 pH meter.

After reaching the adsorption equilibrium, the adsorbent was separated by an external magnetic field. The remaining supernatant was filtered and the concentration of CPF was determined using a standard curve by measuring the absorbance at 290 nm. The %removal of CPF was calculated from eqn (1).

$$\%\text{Removal} = \frac{(C_0 - C_e)}{C_0} \times 100 \tag{1}$$

where C_0 and C_e are the initial and equilibrium concentrations of CPF in mg L^{-1}, respectively.

The amount of adsorbed CPF on the MMIP (a.k.a. adsorption capacity) was calculated according to eqn (2):

$$q_e = \frac{(C_0 - C_e)}{m} \times V \tag{2}$$

where q_e (mg g^{-1}) is the adsorption capacity, C_0 and C_e are the initial and equilibrium concentrations of CPF (mg L^{-1}), respectively, V is the solution volume in litres and m is the adsorbent mass in grams.

Thereafter, the imprinting factor (IF) was calculated as the ratio between the binding capacity of MMIP and that of the corresponding MNIP according to eqn (3).

$$\text{IF} = \frac{Q_{(\text{MMIP})}}{Q_{(\text{MNIP})}} \tag{3}$$

Adsorption kinetics

The pseudo-first-order, PFO, (eqn (4)),[46,48] pseudo-second-order, PSO, (eqn (5))[46,48] and the intraparticle diffusion, IPD, (eqn (6))[48,49] kinetic models were implemented to study the adsorption process of CPF on the surface of the MMIP particles.

$$q = q_e(1 - e^{-k_1 t}) \tag{4}$$

$$\frac{t}{q} = \frac{1}{k_2 {q_e}^2} + \frac{t}{q_e} \tag{5}$$

$$q_t = k_{\mathrm{id}} t^{1/2} + I \tag{6}$$

where q is the adsorption capacity (mg g^{-1}) after a certain contact time, t is time (min), k_1 is the PFO rate constant (L min^{-1}) (k_1 is equal to the slope of a plot of $\ln(q_e - q)$ against t), k_2 is the PSO rate constant (g mg^{-1} min^{-1}) (k_2 can be obtained from the slope and intercept of the straight line obtained by plotting t/q *versus* t), and k_{id} is the intraparticle rate constant (mg g^{-1} $\mathrm{min}^{-1/2}$).

Adsorption isotherms

Freundlich, Langmuir and Temkin isotherms. Studying adsorption isotherms is crucial for understanding the release/retention of an adsorbate to an adsorbent through aqueous media. The adsorption isotherm is a plot that describes the adsorption equilibrium at constant pH and temperature.[48] Langmuir (eqn (7)), Freundlich (eqn (8)) and Temkin (eqn (9)) isotherms are the most common and traditional isotherm models used. Both models were applied in the present study in order to investigate the release/retention of CPF to/by MMIP in aqueous solution.

$$\frac{C_e}{q_e} = \frac{1}{q_{\max} b} + \frac{1}{q_{\max}} C_e \tag{7}$$

$$\log q_e = \log K_F + \frac{1}{n} \log C_e \tag{8}$$

$$q_e = \frac{RT}{b_T} \ln A_T + \frac{RT}{b_T} \ln C_e \tag{9}$$

where q_e (mg g^{-1}) is the equilibrium adsorption capacity, C_e (mg L^{-1}) is the equilibrium concentration, $q_{\max}$ (mg g^{-1}) is the maximum adsorption capacity, b is the Langmuir constant, K_F is the Freundlich adsorption coefficient related to the materials adsorption capacity, $1/n$ is a constant the describes the heterogeneity of the adsorbent surface, R is the universal gas constant, T is the absolute temperature in kelvin, b_T is the Temkin isotherm constant, and A_T (L g^{-1}) is the Temkin isotherm equilibrium binding constant.

In Langmuir isotherm, a linear regression of C_e/q_e *vs.* C_e was plotted to calculate $q_{\max}$ and b constants. Meanwhile, a plot of $\log q_e$ *versus* $\log C_e$ can be used to determine $1/n$ and K_F constants from Freundlich isotherm. Similarly, the slope and intercept of a plot of q_e *versus* $\ln C_e$ in Temkin equation can be used to calculate b_T and A_T constants.

Scatchard plot. By using the Scatchard analysis, the total amount of bound CPF divided by its free concentration (q_e/C_e) was plotted *versus* the total bound amount of CPF, q_e (mg g^{-1}). For a single kind of adsorbent, the slope of the linear plot obtained from Scatchard analysis is equal to $-K$, the association constant for the binding of adsorbate (CPF) to the adsorbent (MMIP), while the x-intercept can be used to calculate the number of binding sites ($B_{\max}$). See eqn (10) below for Scatchard analysis.

$$\frac{q_e}{C_e} = K(B_{\max} - q_e) \tag{10}$$

Hill plot. Hill plots define a saturation fraction, ν, equal to the amount of bound adsorbate (q) divided by the number of binding sites, $q_{\max}$. The value of $\log(\nu/(1-\nu))$ is calculated and plotted against $\log C$, where C is the concentration of the adsorbate CPF (eqn (11)). A slope of $0.1 < Q < 0.9$ is the Hill coefficient, h, and is an index of cooperativity.

$$\log\left[\frac{\nu}{1-\nu}\right] = \log K + h \log C \tag{11}$$

Adsorption thermodynamics

Adsorption thermodynamics was studied by incubating 0.2 g of MMIP in 10 mL of 20 mg L^{-1} CPF solution for the equilibration time while keeping mechanical shaking at 400 rpm. The experiment was repeated at different test solution temperatures (*ca.* 303–333 K). Thereafter, the adsorption equilibrium constant (K_a) was calculated at the studied temperatures from eqn (12); Liu reported that at low concentrations the distribution constant (K_c) is equal to the adsorption equilibrium constant.[50] The obtained K_a values were used to calculate the adsorption thermodynamic parameters (ΔH and ΔS) from Van't Hoff equation (eqn (13)) *via* plotting $\ln K_a$ *vs.* $1/T$. Moreover, the change in Gibbs free energy (ΔG) was calculated from eqn (14).[51]

$$K_c = C_{\mathrm{ad}}/C_e \tag{12}$$

$$\ln K_c = \ln K_a = -\frac{\Delta H}{RT} + \frac{\Delta S}{R} \tag{13}$$

$$\Delta G = \Delta H - T\Delta S \tag{14}$$

where C_{ad} is the concentration of adsorbed CPF, C_e is the equilibrium concentration of CPF, ΔH is the enthalpy change, ΔS is the entropy change, R is the universal gas constant and T is the absolute temperature.

Results and discussion

Characterization of MMIP

The materials synthesized in the present work were characterized by means of the following characterization techniques to confirm the formation of crystalline cubic magnetite crystals and to prove the efficient synthesis of the desired nano MMIP.

FTIR. FTIR analysis is one of the powerful characterization techniques of functionalized/composite nanomaterials. This technique can give valuable information about the presence of certain functional groups in the synthesized nanomaterial; thus, FTIR spectra were recorded to confirm the formation of the imprinted as well as the non-imprinted PANI/SPIONs nanocomposites. The infrared absorption spectra of CPF, PANI, washed MMIP and unwashed MMIP (MMIP-CPF) were recorded over the spectral window 4000–400 cm^{-1}.

The FTIR spectrum of naked SPIONs (Fig. 2) demonstrated a characteristic band at about 580 cm^{-1} corresponding to the Fe–O bond stretching. A sharp band appearing at about 1628 cm^{-1} indicates the presence of a carboxylic-metal (Fe–COO) linkage which may be responsible for the surface negative charges of SPIONs. In addition, the presence of hydroxyl groups

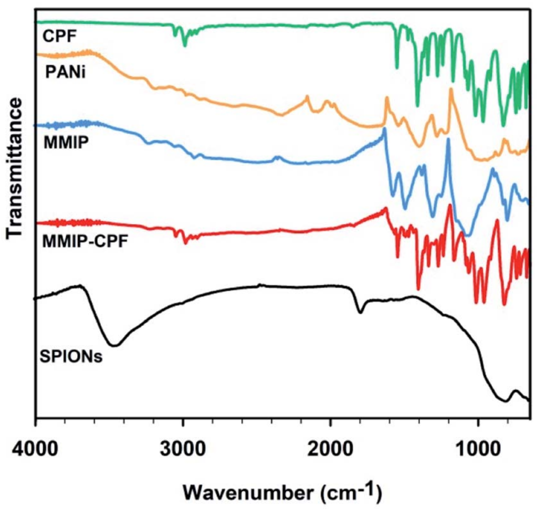

Fig. 2 FTIR spectra of dry solid CPF, SPIONs, PANI, washed MMIP and unwashed MMIP (MMIP-CPF) samples over the spectral window of 4000–400 cm^{-1}.

was confirmed with the broad band appearing at 3650–3000 cm^{-1}.[52]

Confirming the association of PANI with SPIONs necessitates the investigation of the FTIR spectrum of PANI. The synthesis of emeraldine salt of PANI was confirmed *via* the presence of some characteristic bands.[53] For instance, the band at 800–700 cm^{-1} was assigned to C–H in-plane bending and 1,4-disubstituted benzene. The strong broad band positioned around 1000 cm^{-1} is attributed to the bond vibrations of $-NH^+{=}$, $Q{=}NH^+{-}B$, or $B{-}NH^{+\bullet}{-}B$, where B is the benzenoid unit and Q is the quinonoid unit.[53] This band also confirms the dihedral angles distribution between B and Q rings as well as the presence of positively charged moieties in the PANI chain; thus indicating the emeraldine salt structure. In the paper published by Prashar and Nihal,[54] the two absorption bands appearing at 1375 and 1635 cm^{-1} were assigned to the quinonoid and benzenoid rings, respectively. The absorption band demonstrated at 1225 cm^{-1} is due to the C–N$^{+\bullet}$ bond. Moreover, the bands at 1400 and 1545 cm^{-1} are attributed to C═N and C═C stretching vibrations, respectively. The broad absorption band higher than 2000 cm^{-1} is a typical band of conducting PANI.[53] Aromatic C–H stretching was observed *via* the several weak-to-moderate bands appearing at 3300–2880 cm^{-1}. The absence of the hydroxyl band at 3500–3300 cm^{-1} negates the presence of bound water; indicating that the PANI sample was well dried prior to the FTIR measurement. Coming to the FTIR of MMIP, the presence of the absorption band at 580 cm^{-1} is attributed to SPIONs. Moreover, all the above-mentioned absorption bands characteristic to PANI were observed in MMIP spectrum, indicating the successful synthesis of MMIP.

The FTIR spectrum of CPF (Fig. 2) shows characteristic absorption bands at 2986, 1551, 1413, 1272, 1169, 1019, 970, 828 and 674 cm^{-1} that can be assigned to C–H stretching, C–O stretching, C═N stretching, pyridine stretching, ring vibration, ring breathing, P–O–C, P═S stretching and C–Cl stretching, respectively.[55,56] The large similarity between the FTIR spectrum of CPF and that of unwashed MMIP (MMIP-CPF) confirms the successful binding of CPF to the PANI backbone. For instance, all the characteristic CPF absorption bands appear at 2986, 1551, 1409, 1276, 1165, 1019, 965, 828 and 674 cm^{-1} in the MMIP-CPF spectrum. However, after washing of MMIP with a mixture of methanol and 1% acetic acid solution (9 : 1, v/v), these bands almost disappeared and the MMIP spectrum was found to be very similar to that of pure PANI (Fig. 2). The above results depict that MMIP was successfully synthesized and efficiently washed with the washing solution before applying it to the removal of CPF from contaminated water samples.

X-ray diffraction analysis. The XRD analysis was performed to confirm the formation/presence of crystalline magnetite in MMIP samples. To achieve this objective, two samples were analyzed; namely, the as-prepared SPIONs and MMIP. Fig. 3 depicts a typical XRD pattern of cubic crystalline magnetite in both SPIONs and MMIP samples. In case of SPIONS, the diffraction peaks were perceived at 2θ values of 30.1° (220), 35.5° (311), 43.2° (400), 53.5° (422), 57.1° (511) and 62.7° (440).[52,57] The same diffraction angles were obtained in case of MMIP but with a weaker intensity indicating the successful incorporation of SPIONs into the molecularly imprinted PANI matrix. Due to similarities in the XRD diffraction pattern of magnetite (Fe_3O_4) and maghemite (γ-Fe_3O_4), they cannot be distinguished based on their X-ray diffractograms.[58,59] However, according to the literature, the applied method of synthesis is well known to yield magnetite nanoparticles.[60–63]

Magnetic susceptibility. The magnetic properties of SPIONs and MMIP were studied with vibrating sample magnetometry (VSM) where a magnetic field between −20 and 20 kG was applied at room temperature (Fig. 4a). The magnetization hysteresis curve depicts that both SPIONs and MMIP demonstrate superparamagnetic properties as indicated from the high magnetization saturation, and the low remnant magnetization and coercivity values. These excellent magnetic properties may be attributed to the very small size of the prepared SPIONs as will be indicated from the electron microscope images in the

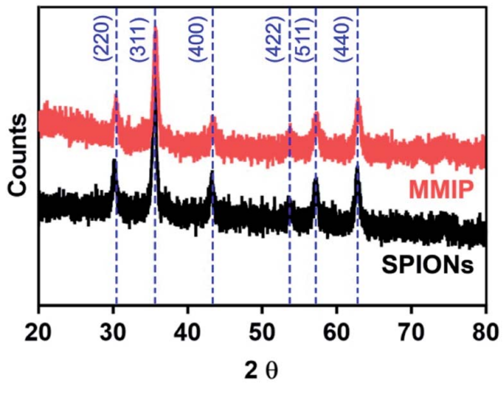

Fig. 3 X-ray diffraction patterns of SPIONs and MMIP samples showing the main diffraction planes of the crystalline phase of cubic magnetite.

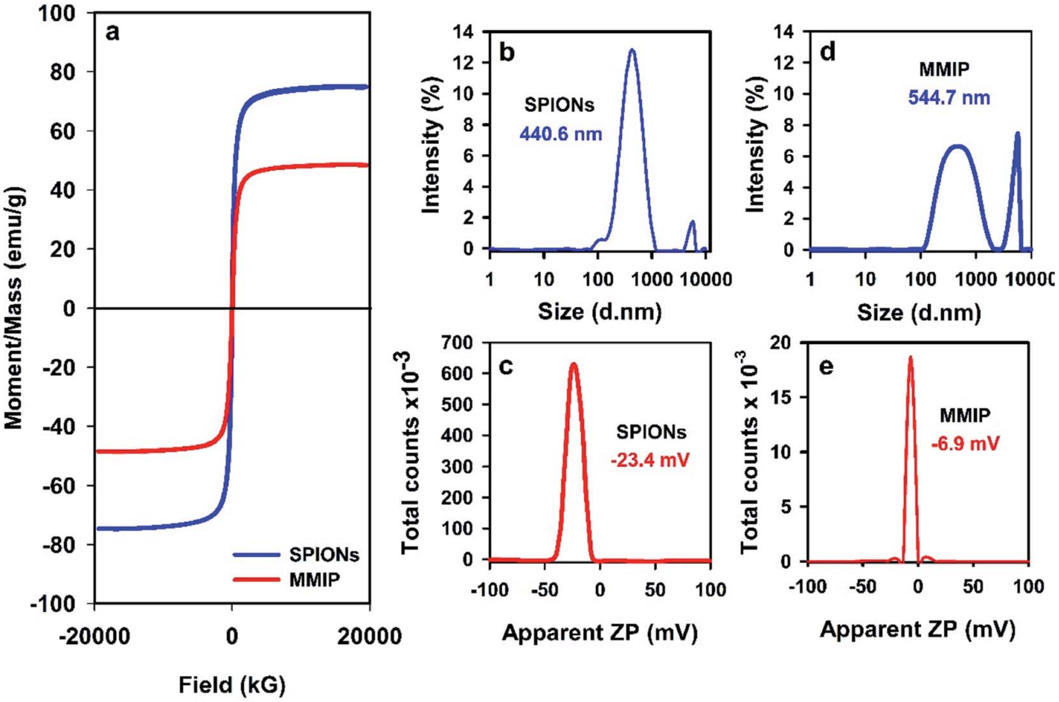

Fig. 4 Magnetization curves (a), dynamic light scattering results (b and d) and surface charges (c and e) of SPIONs and MMIPs.

following sections. Interestingly, MMIP showed a high magnetization saturation (*ca.* 48.42 emu g^{-1}) relatively close to that of the SPIONs counterpart (74.88 emu g^{-1}) indicating that the entrapment of the SPIONs inside the polymeric matrix did not lead to a significant deterioration in their magnetic properties. Therefore, the resulting MMIP can be easily collected by an external magnetic field.

Dynamic light scattering and zeta potential. The size distribution of the as-prepared SPIONs and MMIP was measured using dynamic light scattering (DLS) analysis in a water suspension at room temperature after ultra-sonication for 15 min in a bath sonicator to avoid particles agglomeration. One disadvantage of this technique is its inability to differentiate between single particles and agglomerates, thus it may give false indications of the average particle size especially when the stability of the suspension is not very high. The obtained results (Fig. 4(b) and (d)) show that the average particle size of naked SPIONs and MMIP is about 440.6 and 544.7 nm, respectively. The increase in size indicates the successful incorporation of PANI with the SPIONs to form the MMIP. However, these results must be compared with the results obtained from electron microscopic imaging which gives a more accurate single-particle size.[64]

SPIONs usually bear negative charges on their surfaces due to the presence of carboxylate and hydroxyl functional groups (mentioned above in the FTIR results). Coating of SPIONs with a cationic polymer such as PANI is supposed to increase the positive charges on the surface of the particles, and thus shifts the apparent ZP to a more positive (less negative) value. That is why, the apparent ZP of both SPIONs and the MMIP was measured and the results were plotted as shown in Fig. 4(c) and (e), respectively. Naked SPIONs showed a negative ZP of −23.4 mV, and MMIP revealed a more positive ZP of about −6.9 mV indicating the entrapment of SPIONS into the CPF-imprinted PANI matrix.

Electron microscopy. The removal rate and capacity of an adsorbent are significantly influenced by its physical properties (*e.g.* particle morphology and size) that also dictate the application mode of the adsorbent for water treatment. For example, it was found that minimizing the particle size of activated carbon from 53 μm to 7 μm leads to a shorter equilibrium time for the removal of trichlorophenol (from >200 min to <20 min).[48] Here, particle size and morphology were investigated with electron microscopy imaging. SEM images of SPIONs, MNIP and MMIP are depicted in Fig. 5. The microscopic images of SPIONs (i–iii) show small smooth nanoparticles forming agglomerates. Some of the nanoparticles appear in the form of cubic crystals as shown in Fig. 5(ii) and (iii). In addition, the SEM images of MNIP (Fig. 5(iv)–(vi)) show irregular hair-ice-like structures having rough surfaces with a little porosity compared to naked SPIONs. On the other hand, the SEM images of MMIP depict cancellous/spongy structures, as shown in Fig. 5(viii) and (ix), with highly porous surfaces that may be attributed to the removal of the CPF template from the magnetic imprinted PANI. The size of the produced cancellous/spongy particles is larger than that of naked SPIONs and MNIP (Fig. 5(vii)).

HR-TEM imaging was also used to further confirm the incorporation of SPIONs into the PANI matrix. Naked SPIONs and MMIP samples were imaged using HR-TEM and the obtained images are depicted in Fig. 6. The images show that the

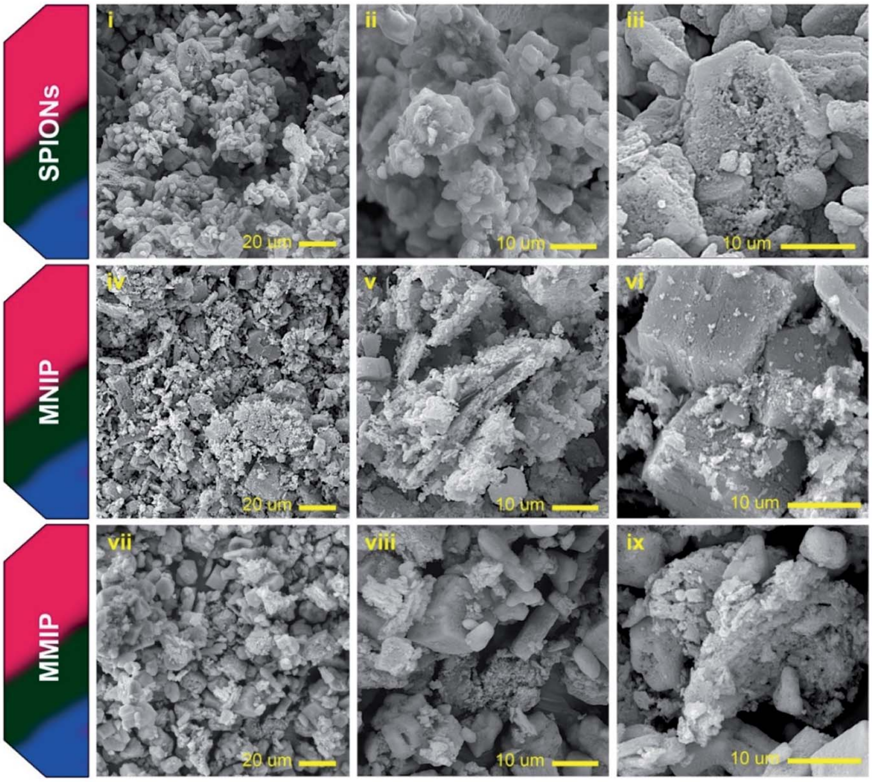

Fig. 5 SEM images of naked SPIONs, MNIP and MMIP with different magnifications.

fabricated SPIONs are spherical and their size ranges from 15 to 30 nm. Fig. 6(iii) shows a group of aggregated SPIONs of a diameter slightly larger than 100 nm, thus confirming the aforementioned DLS results. HR-TEM images of MMIP (Fig. 6(iv) and (v)) demonstrate irregular flakes of PANI embedded with SPIONs of the same size shown in (i), (ii), and (iii), a structure known in the literature as matrix-dispersed structure.[20,46] The images also depict that at least one of the dimensions of the PANI flakes is less than 100 nm in size; hence the name nanocomposite. Fig. 6(vi) depicts the selected area

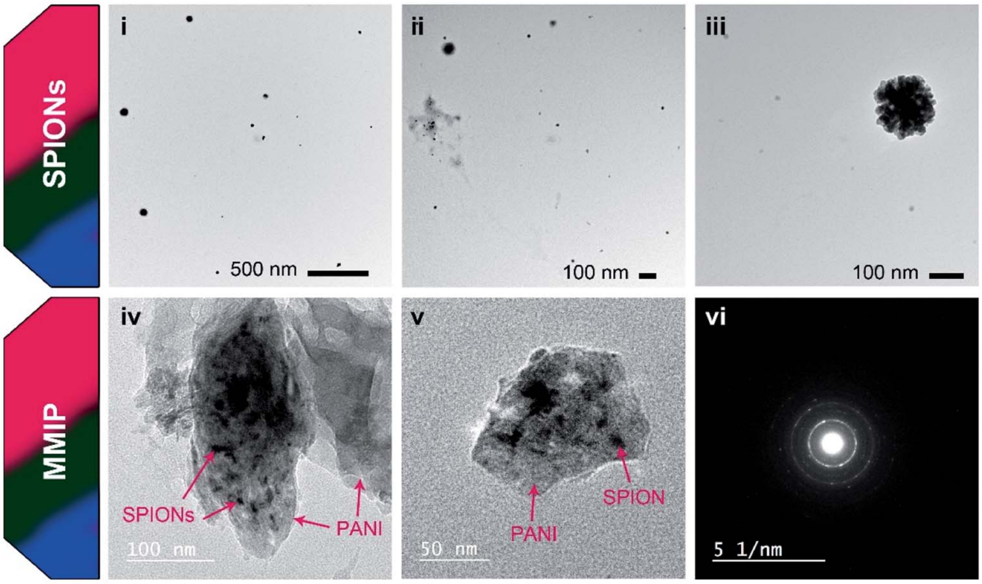

Fig. 6 HR-TEM images of naked SPIONs and MMIP nanocomposite with different magnifications. Panel (vi) shows the SAED pattern of MMIP.

electron diffraction (SAED) pattern of MMIP showing a ring pattern indicating that the fabricated MMIP is a polycrystalline material. The single spots in the SAED pattern may indicate that the MMIP flakes are few nanometers thick. Both SEM and HR-TEM analyses confirm the formation of very small sized SPIONs and SPIONs/PANI nanocomposite.

Adsorption kinetics

The influence of contact time on the CPF removal from spiked water samples is shown in Fig. 7. It is obvious that the adsorption capacity of CPF onto the synthesized MMIP composite nanomaterial increases by increasing the contact time and reaches a plateau after 200 min (Fig. 7b). The mean adsorption capacity of MMIP was found to be 0.27 mg g^{-1}. In other words, about 30% of the CPF content was removed when 10 mL of CPF solution (20 mg L^{-1}) were treated with 0.2 g of MMIP for ≥200 min.

The experiments of adsorption kinetics are usually used to simply supplement the adsorbent evaluation *via* fitting the obtained experimental data to either the PFO or the PSO kinetic models. In addition, studying adsorption kinetics plays a very important role in understanding the adsorption mechanism. The most common empirical models of adsorption kinetics used in studying liquid adsorption are PFO and PSO models. The PSO model often fits adsorption data better than the PFO model as revealed by least-square discrimination. However, the experimental value of q_e is usually higher than the value calculated from the PSO kinetic model, yet very close to it. In the PSO model, the rate of adsorption is mathematically expressed in terms of the occupied adsorption sites (*i.e.* adsorbed amount, q) rather than in terms of the adsorbate concentration. Thus, the changes in the initial bulk concentration of the adsorbate are assumed to be small enough such that they do not influence the kinetic relationship.[65] Interestingly, q_e value calculated from the PSO kinetic model was found to be 0.30 mg g^{-1} which is almost identical to the aforementioned experimental value. In addition, the calculated adsorption rate constant was found to be 9.7×10^{-2} g mg^{-1} min^{-1}. Fitting of experimental data to the PSO kinetic model indicates that CPF chemisorption is the rate-limiting step, and the removal of CPF molecules from bulk solution is due to the physicochemical interactions between CPF and the MMIP surface.[66]

The IPD model further clarifies the removal mechanism of contaminants by newly designed materials, in addition to the PFO and the PSO models. Fig. 7e shows that the adsorption follows a two-stage scenario. Stage 1 represents film diffusion/rapid adsorption which results from the diffusion of CPF through the liquid film surrounding the MMIP surface, whereas the plateau at stage 2 represents the equilibrium stage. The calculated rate constant (k_{id}) was 0.021 and 0.002 mg g^{-1} $min^{-1/2}$ for stage 1 and stage 2, respectively, indicating that the rate of adsorption is faster in case of the former. This can be also confirmed by comparing the values of the intercept (the intercept represents the external resistance to the diffusion of CPF from bulk to the MMIP surface through the boundary layer). Larger intercept values imply a greater effect of the boundary layer. The obtained intercept values are −0.073 mg g^{-1} and 0.243 mg g^{-1} for stage 1 and stage 2, respectively.

Although the PSO model fits the most with the experimental results, diffusion from the bulk must take place in order to

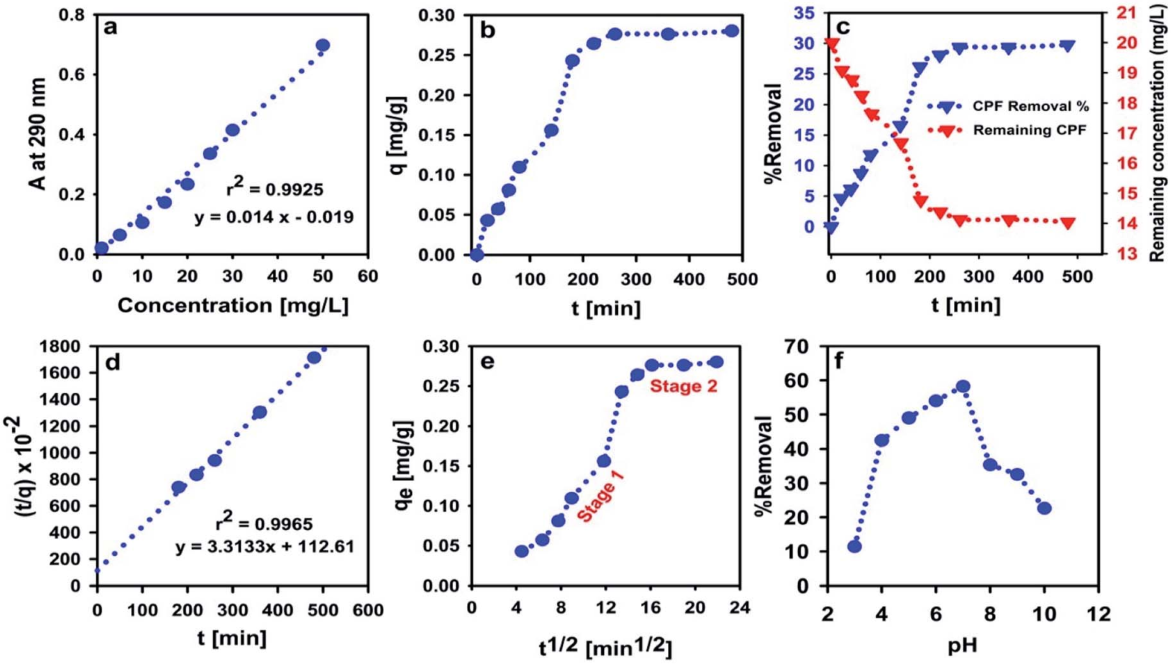

Fig. 7 Calibration plot of CPF aqueous solution at 290 nm (a), influence of contact time on the adsorbent capacity (b) and %removal (c), PSO kinetics of CPF adsorption on MMIP (d), IPD model (e) and the influence of pH on the %removal of CPF (f). All the adsorption experiments were performed in CPF-spiked water samples using the synthesized MMIP.

bring out CPF to the liquid film (*i.e.* thin layer) adjacent to the MMIP surface. Indeed, it is not necessary that this diffusion process is the rate-determining step; hence, the rate-determining step is the physico-chemical process/interaction occurring at the MMIP surface as indicated above from the PSO model.

Effect of solution pH

Studying the effect of solution pH on the rate of removal of water contaminants is very crucial, especially for ionizable adsorbates. Changes in solution pH may enhance or even hinder molecular interactions occurring at the surface of the adsorbent particles due to its significant influence on surface charges. Fig. 7f shows that the highest sorption efficiency is attained at pH 7, while it dropped significantly at higher and lower pH values. In acidic media, emeraldine salt is normally protonated, and thus bearing a large number of positive charges.[67–69] CPF molecule is capable of accepting a proton at pH $\leq$ 10.76, as indicated from its pK_a value. However, the percentage of protonated nitrogen atoms in the PANI chains decreases gradually at pH = 5.5–7.0 giving the partially protonated emeraldine base. Meanwhile, at pH > 7, the number of deprotonated nitrogen atoms in the emeraldine base increases abruptly, leading to the observed decrease in CPF removal shown in Fig. 7f.[69]

These facts suggest that at neutral pH (pH 7), PANI is in the form of the neutral chains of emeraldine base and CPF is protonated bearing a single positive charge per molecule. Indeed, this is the best scenario for adsorption of CPF onto PANI from the electrostatic point of view because it provides the least electrical repulsion forces between CPF molecules and PANI chains. Similar results were obtained by Hamadeen *et al.* in treating CPF-contaminated water with *Moringa oleifera* seed waste.[70] The gradual decrease in the removal percent at pH < 7 confirms that PANI is the main player because it was found that emeraldine salt is a perfect pH-sensitive material which was used for fabricating solid-state pH sensors.[71]

Adsorption isotherms

Adsorption equilibrium takes place when a solution of an adsorbate is brought to contact with the adsorbent particles for a sufficient time until attaining a dynamic balance between the adsorbate bulk concentration and that on the surface of the adsorbent. Adsorption isotherm, a plot that describes the adsorption equilibrium at constant conditions of pH and temperature, is an important tool to predict and/or describe the retention (or release) of an adsorbate to (or from) the surface of an adsorbent.[48] In the present work, Langmuir, Freundlich and Temkin isotherms were used to describe the adsorption of CPF on the surface of the MMIP in aqueous media.

Langmuir isotherm assumes that: (i) adsorption takes place at certain homogeneous sites on the surface of the adsorbent, (ii) the molecules of the adsorbed species do not interact significantly, and (iii) adsorbent saturation occurs after the formation of a single layer of the adsorbate (*i.e.* monolayer coverage).[72] When C_e/q_e was plotted *versus* C_e and the data was regressed linearly, the obtained values of r^2, q_{max} and b were found to be 0.7888, −0.057 mg g^{-1} and −0.06, respectively. The negative values of q_{max} and b indicate the inadequacy of the Langmuir isotherm to describe CPF adsorption onto the MMIP surface.

Freundlich isotherm best fits experimental data resulting from multilayer adsorption to heterogeneous surfaces.[72] The linear correlation coefficient of Freundlich isotherm plot ($r^2 = 0.9713$) suggests that the isotherm fits the experimental data better than Langmuir model (Fig. 8). The calculated n and K_F values are 0.13 and 9.55×10^{-10}, respectively. The small value of n indicates that the adsorption of more CPF molecules becomes difficult/unfavorable as the amount of adsorbed CPF increases on the MMIP surface, thus interpreting the relatively long time required for attaining equilibrium.

Temkin isotherm (Fig. 8c) assumes that the heat of adsorption of all molecules in the layer decreases linearly as a result of increase in surface coverage.[73] The value of the constant b determines the type of the sorption process. When b_T value is <80 000, this indicates physical adsorption. However, the value of the term (RT/b_T), also termed as B, gives information about the heat of adsorption. Values <8 kJ mol^{-1} indicate a weak interaction between the adsorbate and adsorbent molecules at the adsorbent surface.[73] The obtained b_T value is about 677 whereas the B value was found to be 3.66 J mol^{-1}. These values were obtained from a linear plot between q_e and ln C_e with $r^2 = 0.9718$. From regression coefficient values, it is obvious that Temkin isotherm is the equation which best describes the adsorption of CPF onto the MMIP surface. Meanwhile, both Freundlich and Temkin isotherms confirm the involvement of physical adsorption in the governing mechanism of the removal of CPF by the proposed MMIP particles.

Effect of CPF initial concentration

By investigating the influence of initial CPF concentration on the amount of adsorbed CPF onto the surface of MMIP particles (Fig. 8d) it was found that the amount of adsorbed CPF increased from 0.14 to 1.54 mg g^{-1} when the initial concentration of CPF increased from 15 to 45 mg L^{-1}. Indeed, this concentration range is very far from the real concentration present in surface water samples which does not exceed 6.36 mg L^{-1} (*i.e.* CPF solubility in water). These results indicate that the proposed MMIP can be efficiently used for the removal of high dissolved amounts of CPF from environmental water. On the other hand, although the amount of adsorbed CPF on the surface of MNIP particles increases from 0.05 to 1.42 mg g^{-1} by increasing the initial CPF concentration from 15 to 45 mg L^{-1}, it remains below the amount of adsorbed CPF in case of MMIP. This finding confirms the involvement of the selective sites on the surface of MMIP particles in the adsorption process. These sites are not available in case of MNIP.

In order to make a quantitative comparison between CPF-removal efficiency of MMIP and MNIP particles from aqueous solution, the IF was calculated from the adsorption capacity values as mentioned in the Materials and methods section. The

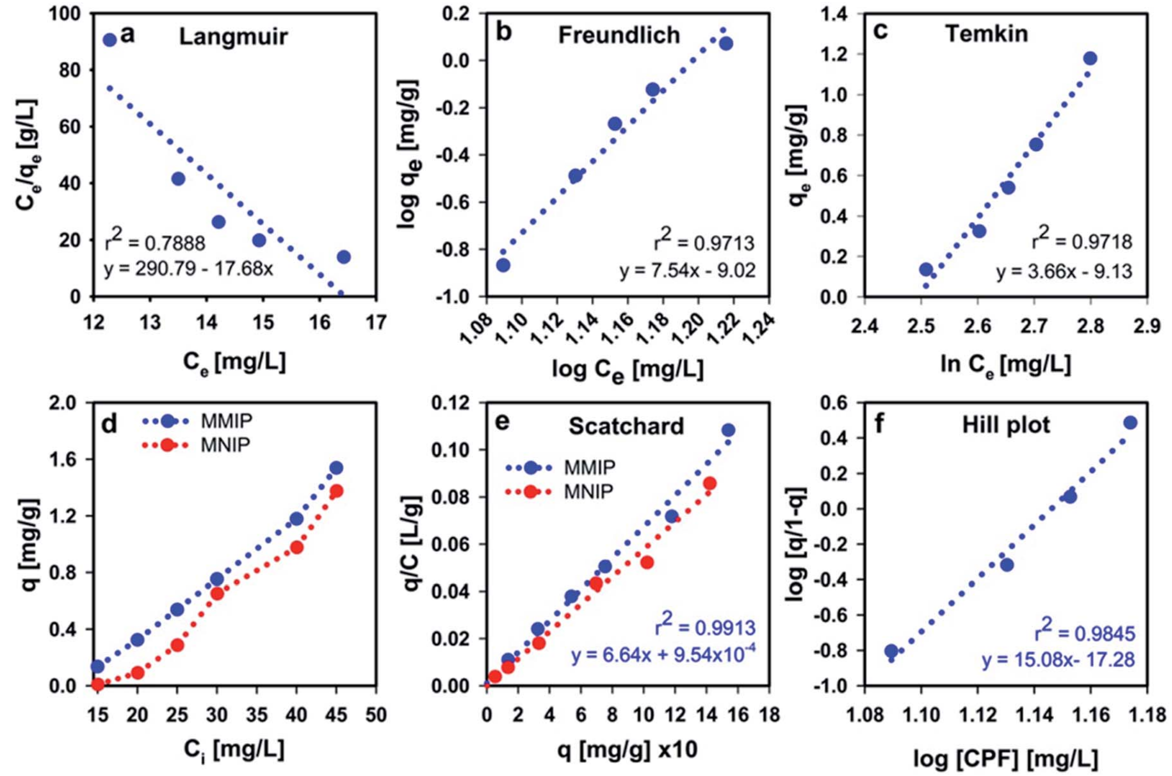

Fig. 8 Langmuir isotherm (a) and Freundlich isotherm (b), Temkin isotherm (c), influence of CPF initial concentration on the adsorption efficiency onto MMIP and MNIP (d), Scatchard plot (e), and Hill plot (f).

obtained IF was found to be 1.64 indicating that the efficiency/selectivity of MMIP in removing CPF from water is 1.64 folds higher than that of the MNIP counterpart.

Scatchard and Hill plots

The Scatchard and Hill analyses are used to study the adsorption processes occurring at the surface of adsorbents. In addition, the Scatchard analysis is often used to determine the affinity of the adsorbate molecules to the adsorbent as well as the number of active biding sites on the surface of the adsorbent. The calculated association constants (K) from Scatchard analysis (Fig. 8e) are -0.066 and -0.058 g L^{-1} for MMIP and MNIP, respectively. Theoretically speaking, the slope of the Scatchard plot should be negative in order to give a positive value for K. However, in 1978, Bowmer and Lindup reported Scatchard plots with positive slopes.[74] Later in 1984, they published another paper attributing the positive value of the slope to the dependence of binding on the concentration of the adsorbate, albumin in their work.[75] They suggested that, increasing the concentration of the adsorbate to a certain extent may reverse the sign of the slope from positive to negative. Henis and Levitzki claimed: "the meaning of the slope in such cases is a complex function of the binding parameters and its exact interpretation depends on the particular model used to analyze the binding data".[76] They analyzed the meaning of the slope of the Scatchard plot in terms of the different allosteric models.[76] The aforementioned information indicates that the dependence of CPF adsorption at the adsorbent surface on the amount of adsorbate is the reason behind the obtained positive Scatchard plots.

Hill plots (Fig. 8f) were first used to interpret the interaction/binding of oxygen to hemoglobin. Although Hill plots are usually drawn only when Scatchard plots are not linear, the slope of Hill plot, h, is an index of cooperativity. The obtained value of h was found to be 15.08 indicating positive cooperativity (occurs when $h > 1.0$). Positive cooperativity means that binding of CPF molecules makes their further binding easier. This is usually attributed to the interaction between the active binding sites at the adsorbent surface such that the binding at one site affects the binding at another.

Adsorption thermodynamics and the effect of temperature

To have a closer insight into the CPF adsorption mechanism at the surface of the MMIP particles, the adsorption equilibrium constant (K_a) was calculated at different test solution temperatures, and then the thermodynamic parameters were calculated. The calculated negative values of ΔG at the studied temperatures indicate that CPF adsorption onto the MMIP particles is a spontaneous process and that CPF molecules tend to stay in the stationary phase. Normally, physisorption is indicated by standard free energy change values (ΔG°) ranging from 0 to -20 kJ mol^{-1}, whereas that of chemisorption ranges from -80 to -400 kJ mol^{-1}.[51,77] The calculated values of ΔG (Table 1) confirm that the adsorption process takes place by

Table 1 Thermodynamic parameters of CPF adsorption on MMIP

T (K)	K_a	Slope	Intercept	ΔH (kJ mol^{-1})	ΔS (J mol^{-1} K^{-1})	ΔG (kJ mol^{-1})
303	2.17	1773.6	−5.07	−14.746	−42.191	−1.955
308	1.99					−1.745
313	1.80					−1.534
318	1.65					−1.323
323	1.07					−1.112
328	0.85					−0.901
333	0.57					−0.690

physisorption. Therefore, the involvement of the imprinted active sites on the MMIP surface is highly acceptable which coincides with the calculated IF.

Moreover, the values of ΔH, ΔS and $T\Delta S$ can be used for expecting the type of interaction taking place at the adsorbent surface. For instance, non-covalent interactions usually include hydrophobic interactions, van der Waals interactions, electrostatic interactions and/or hydrogen bonding. Hydrophobic interactions among nonpolar molecules were proved to be entropy-driven, with $\Delta H > 0$, $\Delta S > 0$ and $\Delta H < T\Delta S$. However, enthalpy-driven processes such as van der Waals interactions and hydrogen bonding usually have $\Delta H < 0$, $\Delta S < 0$ and $|\Delta H| > |T\Delta S|$. Electrostatic interactions-governed adsorption is often characterized by a minor enthalpy and a positive favorable entropy ($\Delta H \sim 0$ or $\Delta H > 0$ and $\Delta S > 0$).[78] The thermodynamic parameters (Table 1) suggest an enthalpy-driven adsorption mechanism *via* van der Waals interactions and hydrogen bonding. These results agree with the results of FTIR spectroscopy. It is worth mentioning that increasing the test solution temperature above 318 K leads to shifting ΔG towards more positive values, thus making the adsorption process unfavorable and significantly affecting the adsorption efficiency. Moreover, the highest removal efficiency was obtained at room temperature (Fig. 9a), making the synthesized MMIP material a promising candidate for removal of CPF from contaminated water at ambient conditions of temperature and pH. This thermal behavior of the adsorption process was observed because the rate-determining step (*i.e.* physico-chemical interaction as indicated from the PSO model) is very sensitive to elevations in solution temperature; unlike covalent interactions which usually show higher thermal stability.

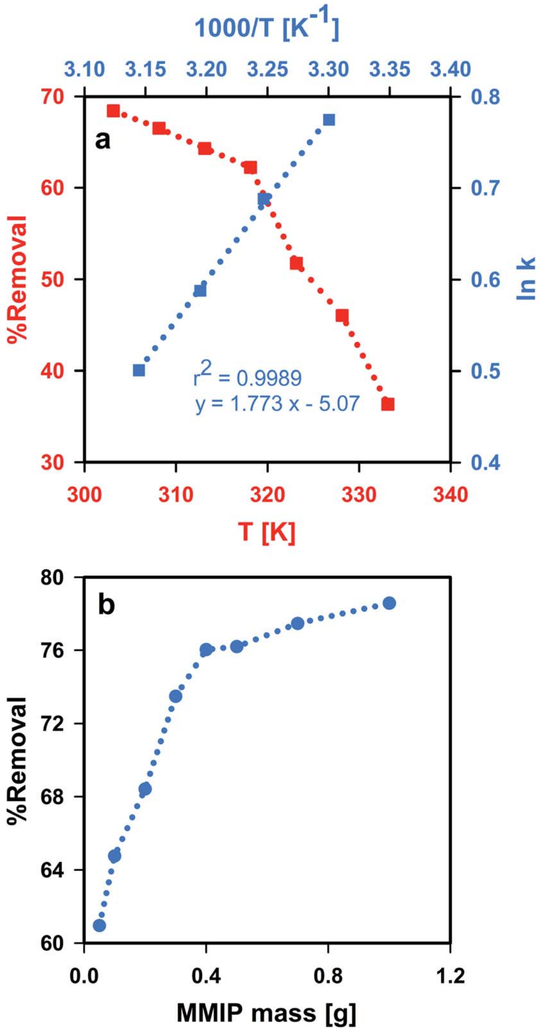

Fig. 9 Thermodynamics and the effect of aqueous solution temperature (a), and the influence of MMIP dose (b) on the adsorption of CPF onto the synthesized MMIP.

Effect of MMIP dose

The amount of MMIP adsorbent (*i.e.* adsorbent dose) was found to significantly influence the removal efficiency of CPF (Fig. 9b). The removal efficiency increased from 61.0 to 78.6% upon increasing the MMIP dose from 0.05 g to 1.0 g. This indicates that the addition of a larger amount of MMIP provides new available active sites for CPF adsorption.

Conclusions

The use of CPF in agriculture represents a serious danger to the environment, especially the freshwater resources, which may act as a possible life threat for both humans, terrestrial and aquatic organisms. Magnetic adsorbents based on MIPs are promising adsorbent materials on account of their selectivity, efficiency, facile large-scale production, safety and ease of separation/control *via* external magnetic field. The present work suggested a novel magnetic molecularly-imprinted polymer material for the efficient removal of CPF from contaminated water. The use of SPIONs in the proposed matrix-dispersed material provided excellent magnetic susceptibility. The suggested MMIP adsorbent was found to attract CPF molecules from bulk *via* van der Waals interactions and hydrogen-bond formation. The adsorption experimental results fitted well to the PSO kinetics model and Temkin adsorption isotherm. Moreover, the most important advantage of this MMIP adsorbent is its selectivity towards CPF in aqueous solution due to the high IF obtained from the adsorption experiments. However, the relatively long time required for adsorption can be shortened by adding more functional groups to the MMIP surface to enhance the interaction with CPF molecules in the bulk. For now, we are trying to investigate the influence of surface functionalization of the proposed MMIP adsorbent, *via* copolymerization, on the equilibration time required for CPF adsorption.

Author contributions

Hadeel Saad: methodology, investigation, formal analysis, writing – original draft, visualization. F. A. Nour El-Dien: supervision, project administration, resources, writing – review and editing. Nadia E. A. El-Gamel: supervision, resources, writing – review and editing. Ahmed S. Abo Dena: conceptualization, methodology, investigation, resources, formal analysis, data curation, visualization, writing – original draft, writing – review and editing.

Conflicts of interest

There are no conflicts to declare.

Notes and references

1 S. M. Maliyekkal, T. S. Sreeprasad, D. Krishnan, S. Kouser, A. K. Mishra, U. V Waghmare and T. Pradeep, *Small*, 2013, **9**, 273–283.
2 A. R. Kulkarni, K. S. Soppimath, A. M. Dave, M. H. Mehta and T. M. Aminabhavi, *J. Hazard. Mater.*, 2000, **80**, 9–13.
3 G. Wulff, A. Sarhan and K. Zabrocki, *Tetrahedron Lett.*, 1973, **14**, 4329–4332.
4 J. J. BelBruno, *Chem. Rev.*, 2019, **119**, 94–119.
5 A. S. Abo Dena, A. M. Ali and I. M. El-sherbiny, *J. Nanotechnol. Adv. Mater.*, 2020, **8**, 1–19.
6 J. Xu, H. Miao, J. Wang and G. Pan, *Small*, 2020, **16**, 1906644.
7 E. Nazarzadeh Zare, A. Mudhoo, M. Ali Khan, M. Otero, Z. M. A. Bundhoo, M. Patel, A. Srivastava, C. Navarathna, T. Mlsna, D. Mohan, C. U. Pittman Jr, P. Makvandi and M. Sillanpää, *Small*, 2021, 2007840.
8 J. Wang, J. Dai, Y. Xu, X. Dai, Y. Zhang, W. Shi, B. Sellergren and G. Pan, *Small*, 2019, **15**, 1803913.
9 R. B. Pernites, S. K. Venkata, B. D. B. Tiu, A. C. C. Yago and R. C. Advincula, *Small*, 2012, **8**, 1669–1674.
10 A. G. Ayankojo, J. Reut, V. Ciocan, A. Öpik and V. Syritski, *Talanta*, 2020, **209**, 120502.
11 T. Beduk, A. Ait Lahcen, N. Tashkandi and K. N. Salama, *Sens. Actuators, B*, 2020, **314**, 128026.
12 M. Sundhoro, S. R. Agnihotra, B. Amberger, K. Augustus, N. D. Khan, A. Barnes, J. BelBruno and L. Mendecki, *Food Chem.*, 2021, **344**, 128648.
13 J. Wang, R. Liang and W. Qin, *TrAC, Trends Anal. Chem.*, 2020, **130**, 115980.
14 H. Y. Hijazi and C. S. Bottaro, *J. Chromatogr. A*, 2020, **1617**, 460824.
15 Z. Zhang, X. Cao, Z. Zhang, J. Yin, D. Wang, Y. Xu, W. Zheng, X. Li, Q. Zhang and L. Liu, *Talanta*, 2020, **208**, 120385.
16 L. A. F. Dinali, H. L. de Oliveira, L. S. Teixeira, W. de Souza Borges and K. B. Borges, *Food Chem.*, 2021, **345**, 128745.
17 M. Guo, Y. Hu, R. Wang, H. Yu and L. Sun, *Environ. Res.*, 2021, **194**, 110684.
18 J. Li, M. Zhu, M. Wang, W. Qi, R. Su and Z. He, *Soft Matter*, 2020, **16**, 7033–7039.
19 L. Fang, Y. Miao, D. Wei, Y. Zhang and Y. Zhou, *Chemosphere*, 2021, **262**, 128032.
20 O. A. Abdel Aziz, K. Arafa, A. S. Abo Dena and I. M. El-sherbiny, *J. Nanotechnol. Adv. Mater.*, 2020, **8**, 21–29.
21 D. S. Cardona, K. B. Debs, S. G. Lemos, G. Vitale, N. N. Nassar, E. N. V. M. Carrilho, D. Semensatto and G. Labuto, *J. Environ. Manage.*, 2019, **242**, 362–371.
22 A. Z. M. Badruddoza, Z. B. Z. Shawon, M. T. Rahman, K. W. Hao, K. Hidajat and M. S. Uddin, *Chem. Eng. J.*, 2013, **225**, 607–615.
23 M. Soylak, O. Ozalp and F. Uzcan, *Trends Environ. Anal. Chem.*, 2021, **29**, e00109.
24 K. Shrivas, A. Ghosale, N. Nirmalkar, A. Srivastava, S. K. Singh and S. S. Shinde, *Environ. Sci. Pollut. Res.*, 2017, **24**, 24980–24988.
25 P. Wang, Y. Yin, Y. Guo and C. Wang, *RSC Adv.*, 2015, **5**, 72572–72578.
26 C. Anudechakul, A. S. Vangnai and N. Ariyakanon, *Int. J. Phytorem.*, 2015, **17**, 678–685.
27 P. Prasertsup and N. Ariyakanon, *Int. J. Phytorem.*, 2011, **13**, 383–395.
28 M. M. Jacob, M. Ponnuchamy, A. Kapoor and P. Sivaraman, *J. Environ. Chem. Eng.*, 2020, **8**, 103904.
29 Y. Samet, E. Hmani and R. Abdelhédi, *Water SA*, 2012, **38**, 537–542.
30 H. Liu, J. Chen, N. Wu, X. Xu, Y. Qi, L. Jiang, X. Wang and Z. Wang, *Ecotoxicol. Environ. Saf.*, 2019, **170**, 259–266.
31 K. Naddafi, S. S. Martinez, R. Nabizadeh, K. Yaghmaeian, S. J. Shahtaheri and H. Amiri, *Water Sci. Technol.*, 2020, **83**, 212–222.
32 J. Femia, M. Mariani, C. Zalazar and I. Tiscornia, *Water Sci. Technol.*, 2013, **68**, 2279–2286.
33 M. Rani and U. Shanker, *Environ. Sci. Pollut. Res.*, 2018, **25**, 10878–10893.
34 S. Vigneshwaran, J. Preethi and S. Meenakshi, *Int. J. Biol. Macromol.*, 2019, **132**, 289–299.
35 A. S. Nair and T. Pradeep, *J. Nanosci. Nanotechnol.*, 2007, **7**, 1871–1877.
36 N. Kumar, N. Narayanan and S. Gupta, *React. Funct. Polym.*, 2019, **135**, 103–112.
37 H. R. Nodeh, W. A. Wan Ibrahim, M. A. Kamboh and M. M. Sanagi, *RSC Adv.*, 2015, **5**, 76424–76434.
38 S. Meseguer-Lloret, S. Torres-Cartas, M. Catalá-Icardo, E. F. Simó-Alfonso and J. M. Herrero-Martínez, *Anal. Bioanal. Chem.*, 2017, **409**, 3561–3571.
39 O. Aydın Urucu, A. Beyler Çiğil, H. Birtane, E. Kök Yetimoğlu and M. V. Kahraman, *J. Ind. Eng. Chem.*, 2020, **87**, 145–151.
40 C. Ayadi, A. Anene, R. Kalfat, Y. Chevalier and S. Hbaieb, *Colloids Surf., A*, 2019, **567**, 32–42.
41 T. E. Milja, V. S. Krupa and T. P. Rao, *RSC Adv.*, 2014, **4**, 30718–30724.

42 F. Saadati, M. Rahmani, F. Ghahramani, F. Piri, H. Shayani-Jam and M. R. Yaftian, *Desalin. Water Treat.*, 2017, **82**, 210–218.
43 M. B. Regasa, T. R. Soreta, O. E. Femi, P. C. Ramamurthy and S. Kumar, *J. Mol. Recognit.*, 2020, **33**, e2836.
44 J. Luo, J. Huang, Y. Wu, J. Sun, W. Wei and X. Liu, *Biosens. Bioelectron.*, 2017, **94**, 39–46.
45 H. Zhao, C. Zhang, D. Qi, T. Lü and D. Zhang, *J. Dispersion Sci. Technol.*, 2019, **40**, 231–238.
46 A. S. Shair, A. S. Abo Dena and I. M. El-Sherbiny, *Spectrochim. Acta, Part A*, 2021, **249**, 119301.
47 O. Melad, H. Alhendawi and M. Fayyad, *Res. Rev.: J. Chem.*, 2014, **3**, 40–47.
48 M. Ateia, D. E. Helbling and W. R. Dichtel, *ACS Mater. Lett.*, 2020, **2**, 1532–1544.
49 G. D. Sheng, D. D. Shao, X. M. Ren, X. Q. Wang, J. X. Li, Y. X. Chen and X. K. Wang, *J. Hazard. Mater.*, 2010, **178**, 505–516.
50 Y. Liu, *J. Chem. Eng. Data*, 2009, **54**, 1981–1985.
51 C. Wu, X. Lou, A. Huang, M. Zhang and L. Ma, *Appl. Clay Sci.*, 2020, **190**, 105566.
52 H. N. Nassar, H. R. Ali and N. S. El-Gendy, *Fuel*, 2021, **294**, 120534.
53 V. Suendo, Y. Lau, F. Hidayat, M. Reza, A. Qadafi and A. Rochliadi, *Phys. Chem. Chem. Phys.*, 2021, **23**, 7190–7199.
54 A. Prashar and Nihal, *IOP Conf. Ser.: Mater. Sci. Eng.*, 2021, **1033**, 12048.
55 P. Goel and M. Arora, *MRS Adv.*, 2020, **5**, 2661–2667.
56 T. Visser, *Infrared Spectra of Pesticides*, CRC Press, London, 2019.
57 A. A. Qureshi, S. Javed, H. M. A. Javed, A. Akram, M. S. Mustafa, U. Ali and M. Z. Nisar, *Mater. Sci. Semicond. Process.*, 2021, **123**, 105545.
58 X. Yang, C. Chen, J. Li, G. Zhao, X. Ren and X. Wang, *RSC Adv.*, 2012, **2**, 8821–8826.
59 C. F. Holder and R. E. Schaak, *ACS Nano*, 2019, **13**, 7359–7365.
60 R. M. Ashour, R. El-sayed, A. F. Abdel-Magied, A. A. Abdel-khalek, M. M. Ali, K. Forsberg, A. Uheida, M. Muhammed and J. Dutta, *Chem. Eng. J.*, 2017, **327**, 286–296.
61 M. Mahmoudi, S. Sant, B. Wang, S. Laurent and T. Sen, *Adv. Drug Delivery Rev.*, 2011, **63**, 24–46.
62 A. Akbarzadeh, M. Samiei and S. Davaran, *Nanoscale Res. Lett.*, 2012, **7**, 144.
63 H. Fatima and K.-S. Kim, *Korean J. Chem. Eng.*, 2017, **34**, 589–599.
64 M. A. Mohamady Hussein, F. G. D. Baños, M. Grinholc, A. S. Abo Dena, I. M. El-Sherbiny and M. Megahed, *Int. J. Biol. Macromol.*, 2020, **162**, 1760–1769.
65 M. A. Hubbe, S. Azizian and S. Douven, *BioResources*, 2019, **14**, 7582–7626.
66 D. Robati, *J. Nanostruct. Chem.*, 2013, **3**, 55.
67 H. Wan and S. C. Yang, *MRS Online Proc. Libr.*, 2007, **965**, 1223.
68 P. M. McManus, S. C. Yang and R. J. Cushman, *J. Chem. Soc., Chem. Commun.*, 1985, 1556–1557.
69 E. Gill, A. Arshak, K. Arshak and O. Korostynska, *Sensors*, 2007, **7**, 3329–3346.
70 H. M. Hamadeen, E. A. Elkhatib, M. E. I. Badawy and S. A. M. Abdelgaleil, *J. Environ. Chem. Eng.*, 2021, **9**, 105376.
71 H. D. Nguyen, T. H. Nguyen, N. V. Hoang, N. N. Le, T. N. N. Nguyen, D. C. T. Doan and M. C. Dang, *Adv. Nat. Sci.: Nanosci. Nanotechnol.*, 2014, **5**, 45001.
72 V. Fierro, V. Torné-Fernández, D. Montané and A. Celzard, *Microporous Mesoporous Mater.*, 2008, **111**, 276–284.
73 T. Z. E. Lee, J. Zhang, Y. Feng, X. Lin and J. Zhou, *IOP Conf. Ser. Earth Environ. Sci.*, 2021, **657**, 12026.
74 C. J. Bowmer and W. E. Lindup, *J. Pharm. Sci.*, 1978, **67**, 1193–1195.
75 L. S. Clegg and W. E. Lindup, *J. Pharm. Pharmacol.*, 2011, **36**, 776–779.
76 Y. I. Henis and A. Levitzki, *Eur. J. Biochem.*, 1976, **71**, 529–532.
77 G. Gereli, Y. Seki, İ. Murat Kuşoğlu and K. Yurdakoç, *J. Colloid Interface Sci.*, 2006, **299**, 155–162.
78 P. D. Ross and S. Subramanian, *Biochemistry*, 1981, **20**, 3096–3102.